




# Off-Center High Velocity Impact on Cylindrical Pipes and Shells

D. Weihs<sup>1</sup> · D. Rittel<sup>2</sup> 

Received: 3 January 2021 / Accepted: 24 March 2021  
© Society for Experimental Mechanics, Inc 2021

## Abstract

Damage to cylindrical shells, such as pipes and structural elements, that results from collision with supersonically moving particles is studied. Unlike existing work, we examine the effects of *off-center impact*, where the impactor hits at an angle to the cylinder diameter at the point of contact. A numerical assessment of damage and perforation patterns is calculated. New types of damage patterns, including cases of breakup and ricocheting impactors are shown and discussed.

**Keywords** Off-center impact · High velocity · Cylinder-sphere · Damage

## Introduction

Cylindrical shells and pipes are an important part of many structures, from space vehicles through cooling systems of industrial plants to liquid transportation systems. Impact by high-speed particles present a danger to the stability and survival of the structure so that much work has been done on damage, and penetration of metallic surfaces by high velocity impactors, see for instance [1–7]. These usually deal with the effects of impact on flat surfaces of different thickness. However curved surfaces present some additional effects. These were mainly studied for penetration and possible perforation and subsequent depressurization of liquid bearing pipes [5–7]. These are all directed at studying impacts normal to a diameter, which we will call *centered collisions*. An *off-center* collision is defined here as the case when the (undisturbed) trajectory of the projectile does not cross the target center of symmetry (Fig. 1a). Actually, most actual impacts will be off-center so that is rather surprising not to see more attention given to this issue in the literature. Off center collisions are mathematically equivalent to oblique impacts, covered in various

studies of sphere collisions with flat plates. Here we study the high-speed off-center collision with cylindrical shells, which is different as there is an azimuthal dependence on the thickness encountered by the sphere. To simplify the problem, we analyze the effect of impact on thin-walled cylinders. As mentioned above, research found in the open literature considers only normal impact in the direction of a diameter, but off-center collisions are much more probable in real life situations.

We use the numerical ABAQUS 2020 finite element code [8] to calculate the damage caused to cylindrical targets hit at various orientations relative to the axes of the cylinder. To emphasize the specific effects of the finite target radius and azimuthal orientation of impact point, we reduce the number of parameters involved. First, we assume an infinitely long cylinder so that the longitudinal location of the collision is not considered. While the longitudinal location of the impact can obviously influence the significance of damage to a finite length pipe, we do not consider it in the present study. Also, we take a simple shape of impactor, a sphere, again to direct attention to the generic damage patterns and assume that the cylinder stays motionless in space during the time of interaction. Finally we take both bodies to be made of aluminum alloy and at equal temperature, taking aluminum 7075 T651 for these computations, as there are well established equations of state and other parameters for this metal. We note here that the selection of the same material for the threat and the target is made in order to highlight the effects of the geometry of the collision.

---

✉ D. Weihs  
dweihs@tx.technion.ac.il

<sup>1</sup> Faculty of Aerospace Engineering and Autonomous Systems Program, Technion, 32000 Haifa, Israel

<sup>2</sup> Faculty of Mechanical Engineering, Technion, 32000 Haifa, Israel

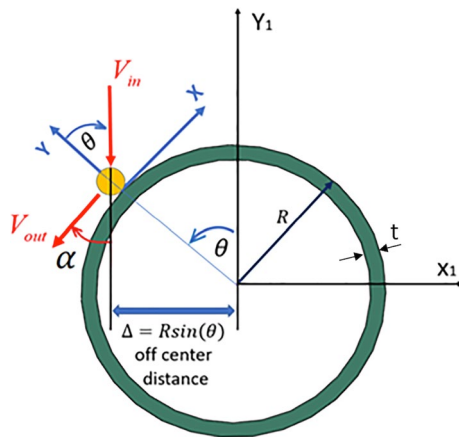


**Fig. 1** Schematic cut description of the off-center impact of a sphere on a cylindrical shell. The vertical red arrow indicates the sphere's undisturbed speed  $V_{in}$ , with  $\theta$  the offset angle.  $V_{out}$  is the velocity of ricochet of the remaining sphere fragment, in cases of non-perforation, and  $\alpha$  is the ricochet angle.  $\Delta$  is the off-center distance

The collisions are at high but not hypervelocity speeds (500 m/s and 1000 m/s), typical of shrapnel and projectile speeds. This results in the effects of the collision to be limited to the close vicinity of the sphere trajectory— an effect known as “punch-through” [9]. This precludes the larger scale denting deformation of the pipe which occurs at steady interactions, or low speed collisions [10].

We show here that off-center impacts result in asymmetric damage patterns. For cylindrical thin-walled pipes, this reduces, by definition, the depth of penetration, so that the point of impact affects the survivability of such bodies, as perforation will require higher energy.

## The Numerical Model

We use the ABAQUS 2020 commercial finite element code [8], run on 2 processors with 8 cores each. The calculations shown here were validated by comparison with experimental data from the literature [11], as described in our recent paper on glancing collisions on a softer aluminum alloy, 6061-T6 [12]. The selection of a different (stronger) aluminum alloy in this work is not deemed to affect the accuracy of the numerical procedures utilized in this work.

We apply a transient adiabatic explicit solution. The model solved in a cut view is shown in Fig. 1. The geometrical dimensions are shown in Fig. 1 where  $D$  is the outer shell

diameter,  $d$  is the sphere diameter and  $t$  is the wall thickness. The length  $L$  we took of the shell section is shown in Fig. 2b.

The mesh we use is shown in Fig. 2. We calculate a typical case, with sphere diameter  $d = 12$  mm. The thickness of the shell is:  $t = 6$  mm and its diameter:  $D = 120$  mm. The length is  $L = 250$  mm, which can be shown to be long enough to simulate an infinitely long cylinder. A top view of the mesh is shown in Fig. 2a with a detail of the top view around the sphere in Fig. 2b. A meshed cut view near the impact location is shown in Fig. 2c. The mesh is comprised of 382,224 elements of type C3D8R (reduced integration and hourglass control) and 417,157 nodes. The mesh seed size on the shell at the impact location is 0.5 mm.

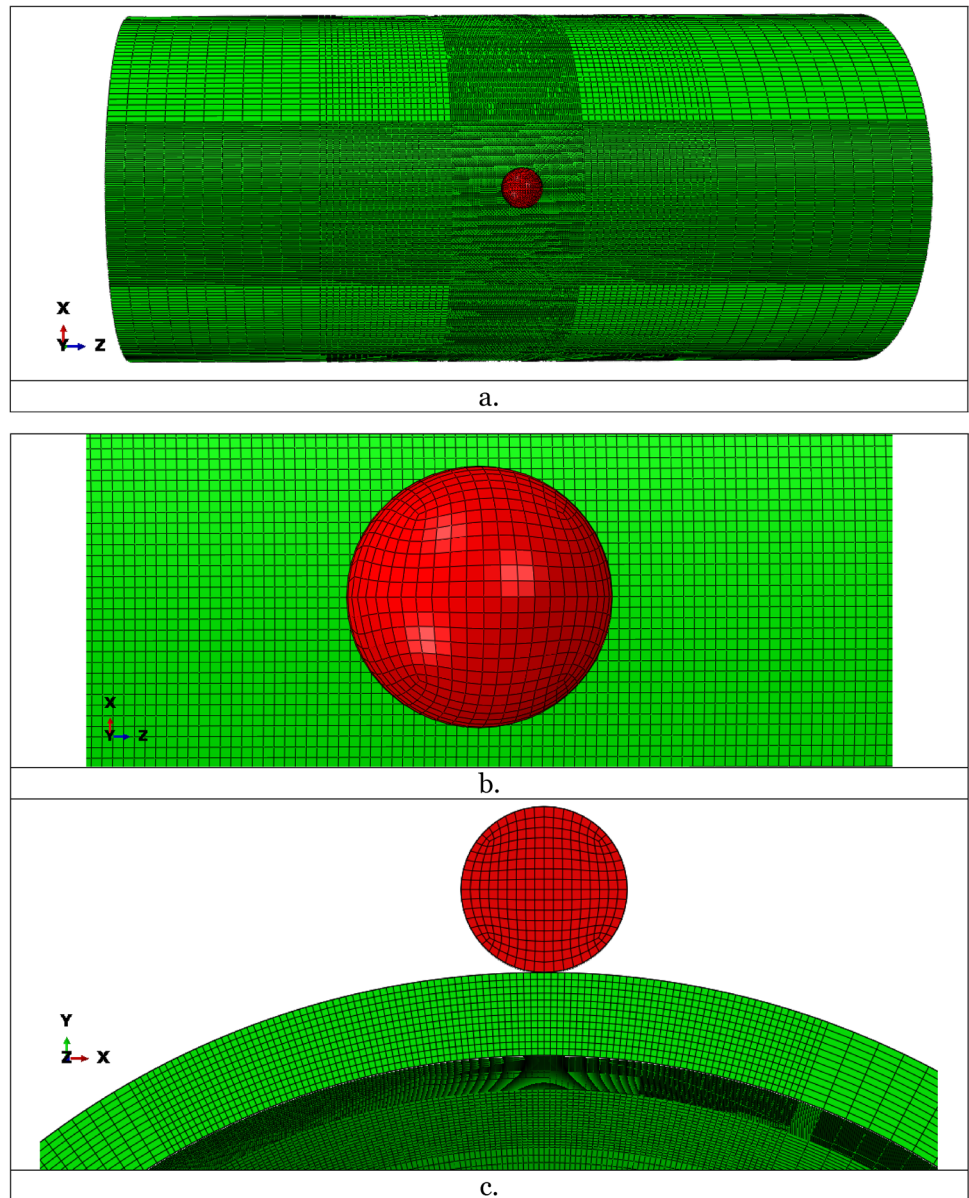
A mesh convergence test was carried out as detailed in Appendix A.

As mentioned in the Introduction, we look at collisions of a stationary cylinder impacted by a fast-moving projectile where both are made of the same material—Aluminum 7075 T651. The material model and parameters (Johnson Cook plasticity and failure) are detailed in Appendix B. Initially, all faces are free and only the sphere has initial velocity. During penetration and erosion, we assume Coulomb friction with a dynamic coefficient of friction 0.3, as obtained from the literature. While the actual penetration process is completed after about 50  $\mu$ s, the analysis is performed until 200  $\mu$ s after initial impact, to show the impactor trajectory after end of the sphere-cylinder contact.

## Results

A typical result in which we select several frames of the time dependent calculation is shown in Fig. 3. The trajectory shown is for an off-center impact of  $\theta = 60^\circ$  ( $\Delta = R \sin(60) = 52$  mm) at a relative speed of 1000 m/s. This figure depicts the main effects of off-center collisions, including asymmetric damage, and the corresponding deflection of the remaining part of the projectile. Isometric views of the sphere and shell are shown on the left column of Fig. 3. Isometric detail views of the impact location are shown in the middle column. Detailed cut views are shown in the right column of Fig. 3. While we determined which material elements of both impactor and target reach failure and are thus deleted, we did not keep track of their trajectories as they probably end up as spall and possibly undergo some reattachment to the crater, so that the ejecta are not characterized in this work.

**Fig. 2** **a** Top view of the cylindrical shell and the spherical projectile (centered impact). **b** A detail of the top view around the sphere. **c** A meshed cut view near the impact location



As mentioned earlier, two impact velocities of the sphere were considered, namely 500 m/s and 1000 m/s. Six off-center locations for which  $\theta = 0^\circ, 15^\circ, 30^\circ, 45^\circ, 60^\circ$  and  $75^\circ$ , respectively, were calculated. The 12 cases are numbered and summarized in Table 1.

In order to quantify the damage (crater sizes) caused by off-center collisions, we define in Fig. 4 the length, width and depth of the crater. The damaged cylindrical shell of case 11 (from Table 1) is shown in Fig. 4a for illustration. A detail of the crater is shown in Fig. 4b, c. The length is the maximum distance between crater points along the

circumferential direction. The width is the maximum distance between crater points along the longitudinal direction. The depth is the maximum distance between crater points along the radial direction.

Table 1 shows the size of the craters for the two different impact speeds for off-center angles  $\theta_i = 0^\circ, 15^\circ, 30^\circ, 45^\circ, 60^\circ$  and  $75^\circ$  which correspond to offset displacement of  $R \sin(\theta_i)$  (see also Fig. 1).

The data of Table 1 is plotted in Fig. 5 to enable seeing the trends. The points show the calculated values, the solid lines represent spline smoothing of the data (note the

**Fig. 3** The trajectory of a  $D = 12$  mm aluminum sphere colliding with a 6 mm thick, 120 mm diameter aluminum alloy pipe at an off center collision at displacement of angle  $\theta$  (see Fig. 1) and a speed of 1000 m/s. The projectile is abraded but does not perforate the pipe, and the remaining fragment is deflected. Times shown are measured from first contact. Note the ricochet angle  $\alpha$  at  $60 \mu\text{s}$  between the initial and final velocity

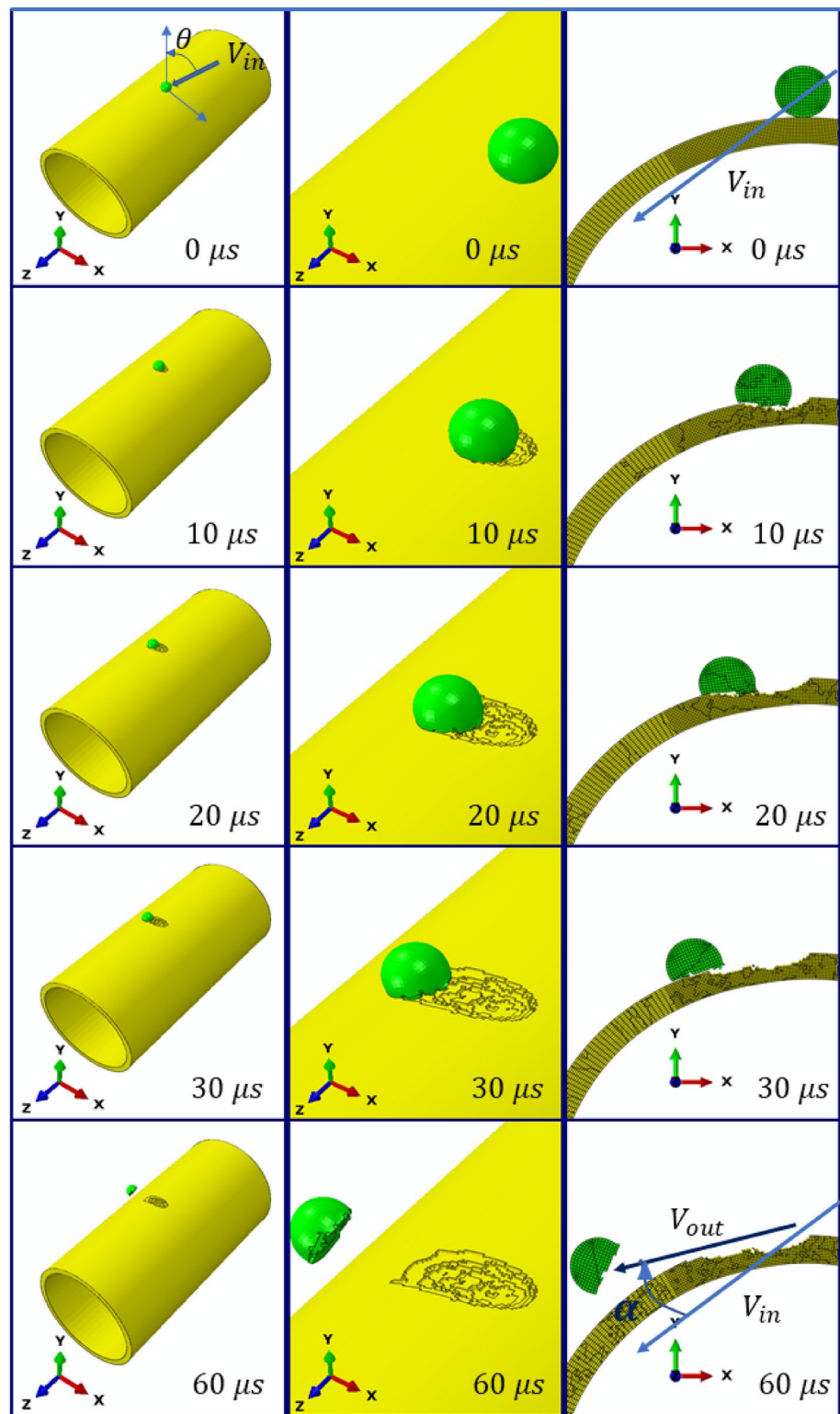




**Table 1** The size of the crater produced by a 12 mm diameter Aluminum 7075 T651 sphere colliding with a 120 mm diameter, 6 mm thick Aluminum pipe of the same material at impact speeds of 500 m/s and 1000 m/s at  $\theta=0^\circ, 15^\circ, 30^\circ, 45^\circ, 60^\circ$  and  $75^\circ$ 

Case	V m/s	$\theta^\circ$	Length (mm)	Width (mm)	Depth (mm)
1	500	0	12	12	3
2	500	15	16	12	3
3	500	30	16	12	3
4	500	45	20	12	3
5	500	60	24	11	1.6
6	500	75	17	6	0.1
7	1000	0	13	13	6
8	1000	15	14	13	6
9	1000	30	18	13	6
10	1000	45	28	13	5
11	1000	60	27	12	3
12	1000	75	18	9	1.5

different scales of each part). The dashed line represents margins of error. Since the element size is 0.5 mm the error margin for the spatial dimensions is assumed to be  $\pm 0.5$  mm. The crater dimensions due to both impact velocities are plotted in Fig. 5 Lengths in 5a, width in Fig. 5b and depths in Fig. 5c.

For centered collisions the crater length is approximately equal to the projectile diameter, with full penetration achieved at between 500 and 1000 m/s. Actually for this case, we found that full penetration is achieved at about 720 m/s. Full penetration is achieved at 1000 m/s for angular displacements of up to  $30^\circ$ . Figure 5 also indicates that for  $\theta > 50^\circ$ , the dimensions of the craters decrease rapidly. This is due to a ricochet effect which interrupts the penetration

process, deflecting the remaining mass of the sphere, as well as causing this mass to rotate due to the asymmetric impact (see Fig. 3).

Top views of the craters for impact speed of 500 m/s are shown in Fig. 6. The sphere moved from right to left in this figure. The figure is a 2D visualization of Fig. 5a, b where the widths and lengths are detailed. It can be observed that, as expected, with increasing  $\theta$ , the crater becomes elongated shallower and asymmetric.

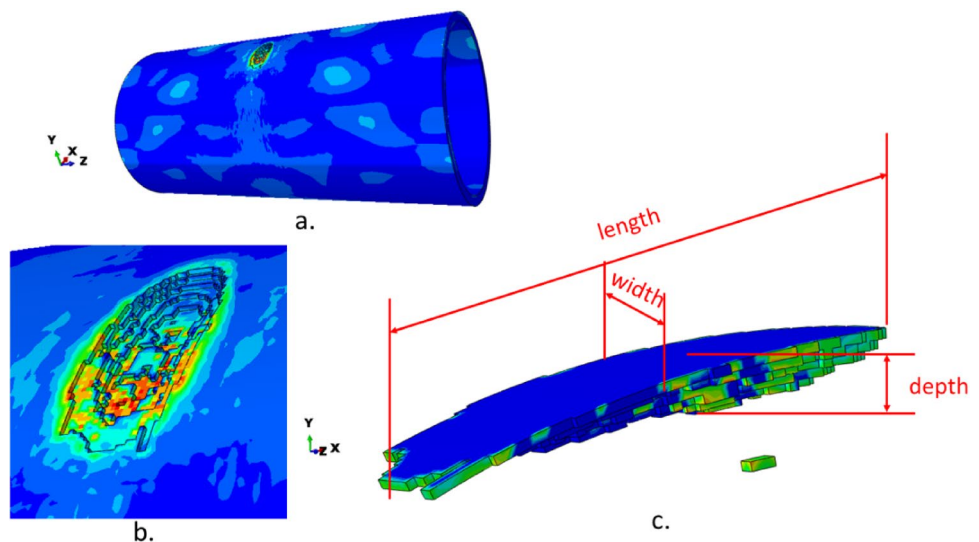
Table 2 tabulates the failed mass (equivalent to volume) of the sphere, cylinder and total for all the 12 cases solved.

To visualize the asymmetric erosion with increasing off-center angle  $\theta$ , we show the undeformed failed elements of the sphere and shell due to impact locations at  $\theta=0^\circ, 15^\circ, 30^\circ, 45^\circ, 60^\circ$ , and  $75^\circ$  and impact velocity of 1000 m/s. With usage of the “undeformed” option, the elements are shown in their initial position prior to the impact in Fig. 7. For increasing  $\theta$ , the asymmetric encounter results in less erosion of the projectile while the erosion of the target shell becomes asymmetric, from cylindrical perforation to elongated crater.

The initial total energy of the shell-sphere system is the kinetic energy of the sphere. Let's examine (for example) the energy partition of case 11 in Fig. 8 after normalizing by the initial kinetic energy of the sphere.

During a relatively short initial period of *ca.* 25 ms, a significant part of the initial energy ( $\sim 40\%$ ) gets dissipated, while energy is transferred from the sphere to the shell. This initial period corresponds to the direct sphere-shell interaction (penetration and fragmentation), beyond which the remaining energies become relatively constant. A detailed account of all the various characteristic energies of the system can be found in Appendix C.

**Fig. 4** The damaged cylindrical shell due to impact of a 12 mm diameter sphere at 1000 m/s at  $\theta=60^\circ$  (case 11 Table 1). **a** The whole damaged cylindrical shell. **b** The crater. **c** The undeformed failed elements of the crater with definition of length, width and depth of the crater. The color code for the von Mises stresses appears in Fig. 11 (Appendix A)



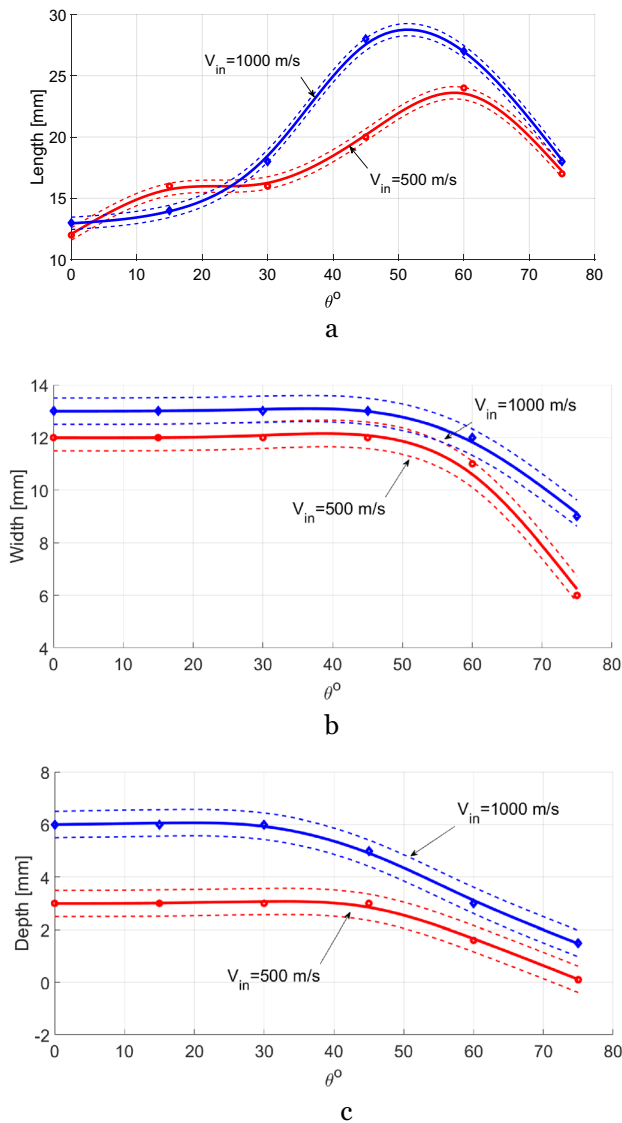


**Fig. 5** Crater dimensions due to “off center” impact of a 12 mm diameter sphere on 120 diameter cylindrical shell with 6 mm thickness. Two impact velocities of 500 m/s and 1000 m/s at off-center angle  $0 \leq \theta \leq 75^\circ$ . **a** Lengths, **b** Widths, and **c** Depths. The solid lines are obtained by connecting calculated points, while the dashed lines indicate the range of uncertainty (error)

The total internal and kinetic energy of the sphere and shell only include  $\sim 60\%$  of the initial kinetic energy, of which about 20% is stored within the elements of the impacting sphere while the rest,  $\sim 40\%$ , is transferred to the cylindrical shell.

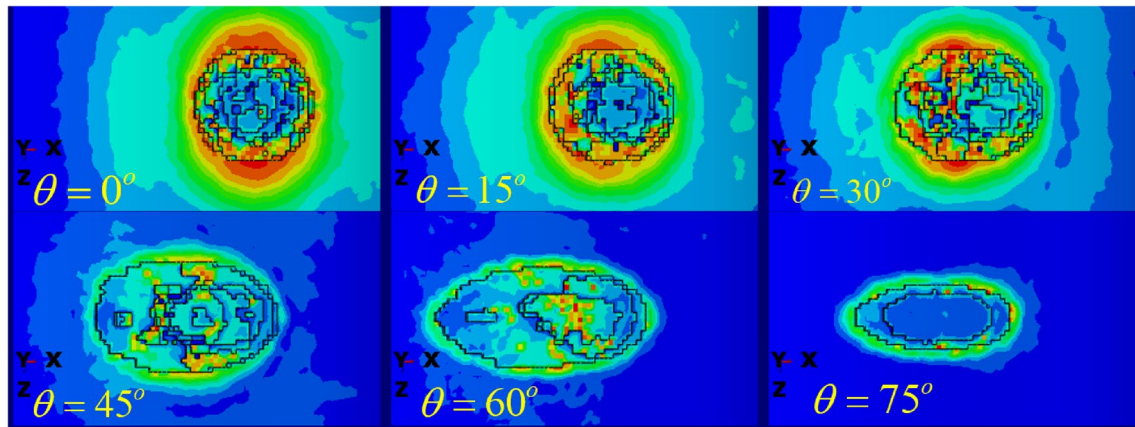
Next, consider the azimuthal dependence of the impact on the energies. The remaining energy within the sphere, shell and the whole assembly of the sphere and shell (named “total”) for different off center azimuths ( $0^\circ \leq \theta \leq 75^\circ$ ) is shown in Fig. 9. The energy is normalized by initial kinetic energy of the sphere. A comparison between impact velocities of 500 m/s and 1000 m/s is detailed. The remaining normalized energy within the impacting sphere is shown in Fig. 9a. The transferred remaining normalized energy to the cylindrical shell is shown in Fig. 9b. The total remaining normalized energy which is the sum of the remaining normalized energy of the shell and sphere is shown in Fig. 9c.

Figure 9a reveals that the part of the energy remaining in the sphere increases for  $\theta > 40^\circ$ . The reason is that for these angles, ricocheting occurs and more of the kinetic energy of sphere is preserved and not transferred to the shell target.

Likewise, for  $\theta > 40^\circ$ , it is observed in Fig. 9b that the remaining energy within the shell target drops more rapidly. Ricocheting at these angles decreases the energy transfer from the impacting sphere to the target. It can be concluded that for maximum energy transfer to the target, higher impact velocities at locations of  $\theta < 40^\circ$  are desirable.

The total remaining normalized energy which is shown in Fig. 9c ranges between 55 and 94% with a slight minimum value reached at  $\theta \cong 40^\circ$ .

Figure 10 shows the variation of angle of ricochet of the sphere’s residual mass with the initial offset angle. Past an offset angle of some  $30^\circ$ , the ricochet angles  $\alpha$  assumes a low value irrespective of the sphere velocity, just equivalent to the impactor “caressing” the shell with minimal damage.



**Fig. 6** Damage top view for a 12 mm Aluminum sphere colliding with a 6 mm thick, 120 mm diameter 7075 T651 Aluminum pipe at various off-center displacements ( $0 \leq \theta \leq 75^\circ$ ) at a speed of 500 m/s. The color code for the von Mises stresses appears in Fig. 11 (Appendix A)

**Table 2** Failed mass for cases 1–12

Case	$V_{\text{sphere}}$ (m/s)	$\theta^\circ$	Mass failed and deleted		
			$M_{\text{sphere}}$ (g)	$M_{\text{cylinder}}$ (g)	$M_{\text{total}}$ (g)
1	500	0	0.56	0.75	1.3
2	500	15	0.55	0.73	1.3
3	500	30	0.51	0.71	1.3
4	500	45	0.44	0.64	1.1
5	500	60	0.26	0.44	1.1
6	500	75	0.002	0.21	0.21
7	1000	0	1.40	1.8	3.2
8	1000	15	1.4	1.8	3.2
9	1000	30	1.5	1.7	3.2
10	1000	45	1.3	2.1	3.4
11	1000	60	0.71	1.0	3.4
12	1000	75	0.15	0.28	0.43

## Discussion

The damage due to the lateral distance between the sphere trajectory and the pipe centerline changes dramatically as this distance increases. As a specific example, for an impact velocity of 1000 m/s, normal and up to  $30^\circ$  offset the shell is penetrated (depth of 6 mm, i.e., the full wall thickness). The depth of penetration is reduced as the lateral displacement of the projectile trajectory increases, while the crater

is elongated. This results from both the larger effective thickness encountered by the sphere, and the asymmetric resistance of the pipe material due to the curvature of the pipe at these locations. This asymmetric encounter results in the projectile being eroded asymmetrically (Fig. 3). For the same impact energy (collision velocity) at small offsets, the projectile perforates the pipe while for larger displacements, it gets embedded in the pipe wall, and at even larger offsets, the remaining fragment is deflected away from the pipe and moves sideways. This deflection appears in Fig. 9, which shows the variation of angle of deflection of the sphere residual mass with the initial offset trajectory, which we see as a ricochet effect. We see that in our cases, offsets of some  $30^\circ$  for both 500 m/s and 1000 m/s minimize the projectile's ricochet effect.

Some further relevant parameters calculated in the present study are summarized in Table 3, for both the target and the projectile, the various energies involved and the ricochet-ing angle.

As a final remark, one should keep in mind that this work presents preliminary results about off-center impact effects, as exemplified by two impact velocities, one sphere diameter and a single target annular wall-thickness. The subject and the methodology developed here are important enough to motivate further studies and include more combinations of parameters resulting in a more general picture.

**Fig. 7** Damage due to impact velocity of 1000 m/s with impact locations at  $\theta = 0^\circ, 15^\circ, 30^\circ, 45^\circ, 60^\circ$ , and  $75^\circ$ . **a** The undeformed eroded sphere and shell. **b** The undeformed eroded elements of the sphere and shell

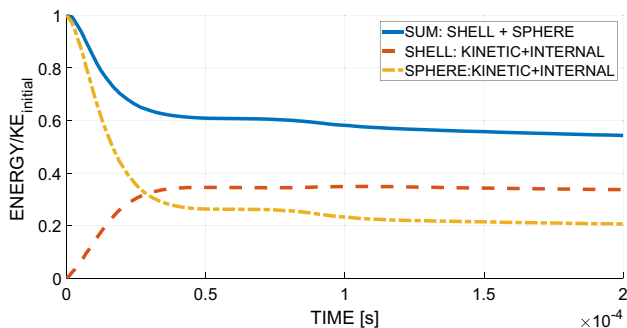
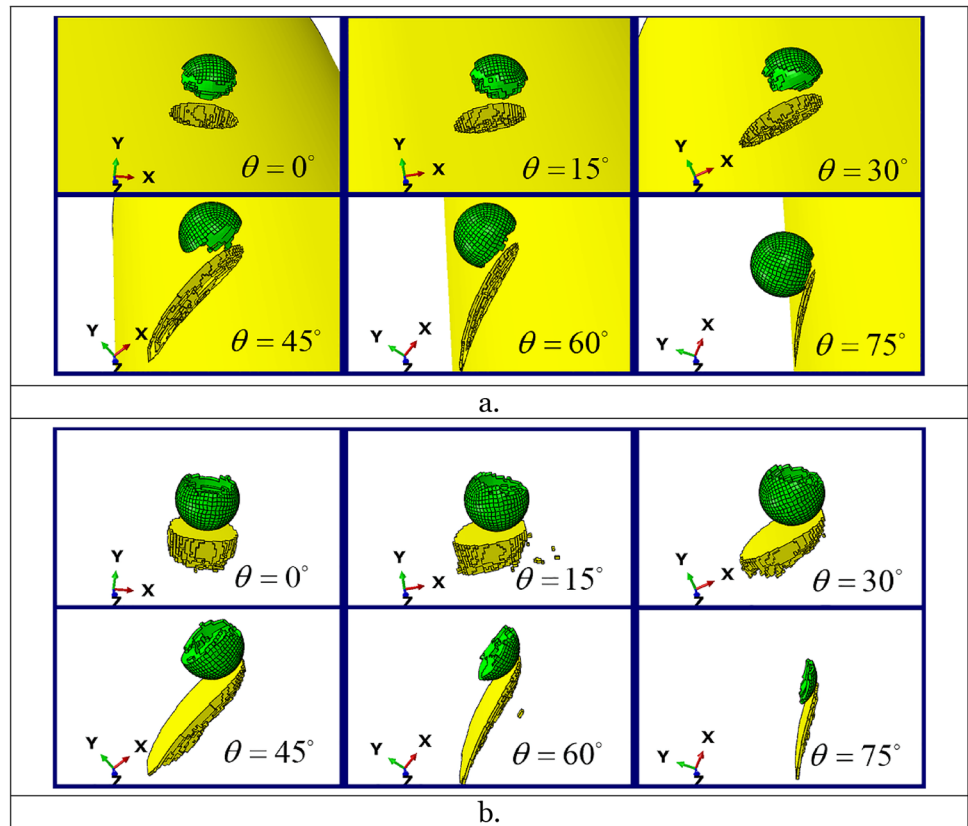


**Fig. 8** Energy partition: the normalized sum of internal and kinetic energy within the sphere and the cylindrical shell during collision of a 12 mm Aluminum sphere with a 6 mm thick, 120 mm diameter Aluminum pipe at various off center displacements ( $\theta = 60^\circ$ ) at a speed of 1000 m/s

## Conclusions

We show here that the actual point of contact of a projectile moving perpendicular to a cylindrical pipe has a tremendous effect on the outcome of the collision. This point has not

been stressed enough, if at all, in the existing literature. The collisions we study are at high speed, where the effect is limited to a small area of order projectile diameter leaving the rest of the shell unchanged. To be conservative, we use a sphere to represent the projectile.

As the lateral distance between the pipe centerline and the impactor trajectory grows, the damage is reduced, and spread over a larger area (Fig. 3). As a result, for the same combination of projectile and target, including the speed of collision, we get a wide range of effects. These include perforation and even damage to the far-side inner wall, through deep, non-penetrating, gouging of the wall, all the way to slight damage and deflection of the sphere. This highlights the importance of the exact configuration during impact on its consequences.



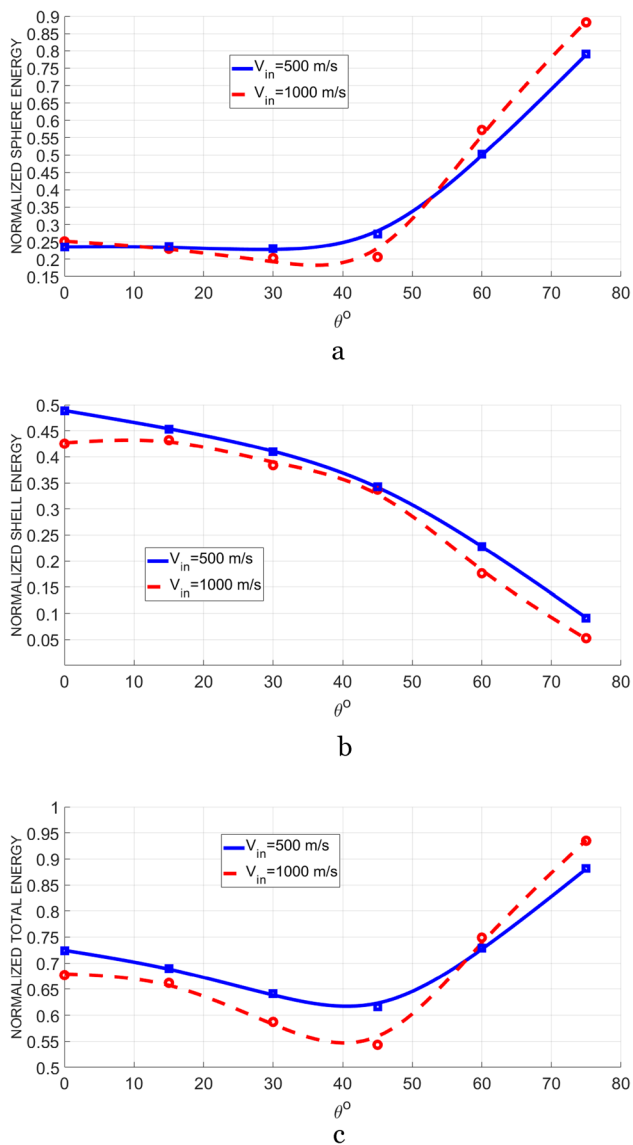


**Fig. 9** Remaining normalized energy partition for impact velocities of 500 m/s and 1000 m/s for  $0^\circ \leq \theta \leq 75^\circ$ . **a** Energy within the sphere. **b** Energy within the cylindrical shell. **c** The total remaining energy within the sphere and shell

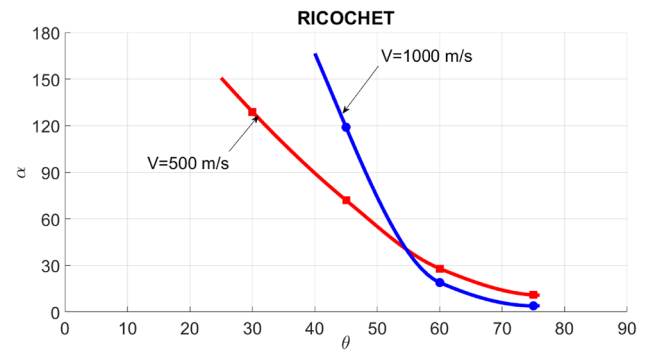


**Fig. 10** Ricochet angle of the remaining fragment of the sphere.  $\theta$  is the off-center angle (see Fig. 1) and  $\alpha$  is the ricochet angle—( $\alpha = 0^\circ$  means that there is no ricochet). The solid lines are obtained by connecting calculated points

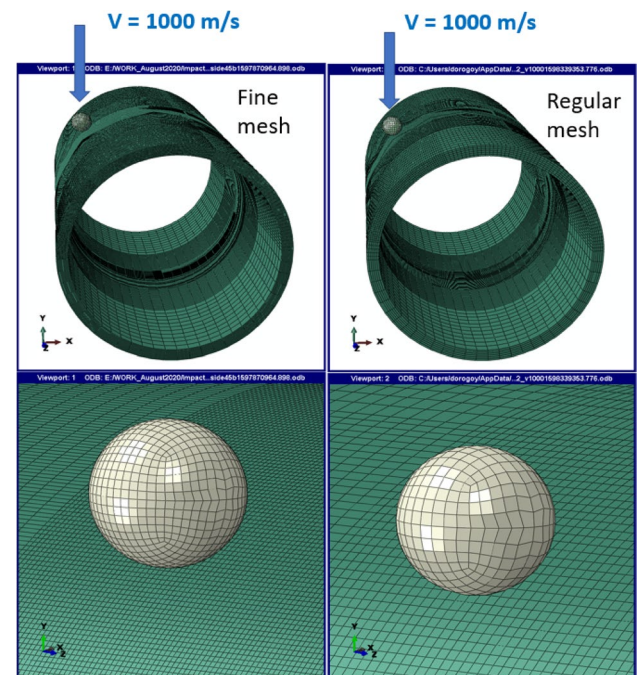


**Fig. 11** The geometry and mesh. The coarser mesh is on the right and the finer mesh is on the left. Details are shown on the bottom of the figures

**Table 3** The normalized (%) final plastic dissipation and residual kinetic energy of the cylindrical shell and sphere for the 12 cases of Table 1. The energies are normalized by initial kinetic energy of the sphere. The ricochet angle is also detailed

$V_{in}$ (m/s)	Off center $\theta^\circ$	Cylindrical shell		Sphere		Ricochet $\alpha^\circ$
		Plastic dissipation (%)	Kinetic energy (%)	Plastic dissipation (%)	Kinetic energy (%)	
500	0	24.4	11.7	15.4	3.8	—
500	15	23.3	9.6	15.6	3.5	—
500	30	21.5	8.0	14.9	3.7	129
500	45	18.6	5.3	12.8	10.2	72
500	60	12.5	3.1	7.3	39.9	28
500	75	4.9	1.4	0.8	77.8	10
1000	0	21.3	13.5	9.6	12.7	—
1000	15	22.7	12.5	10.3	9.6	—
1000	30	21.7	8.7	11.2	6.2	—
1000	45	17.1	9.0	10.9	7.0	119
1000	60	7.9	6.2	5.7	50.1	19
1000	75	2.5	1.9	1.2	86.6	3

**Table 4** Physical properties, JC dynamic failure properties and JC dynamic failure properties for Aluminum 7075 T651 [13–15]

Reference density (Kg/m <sup>3</sup> )	Shear modulus, G (GPa)	Reference temperature, $T_r$ (K)	Melting temperature, $T_m$ (K)	Inelastic heat fraction, $\beta$	Specific heat (J/Kg K)
2810	26.96	293	750	1.0	960
A, (MPa)	B, (MPa)	n	m	C	$\dot{\epsilon}_0$
527	575	0.72	1.6	0.0075	0.00016
$d_1$	$d_2$	$d_3$	$d_4$	$d_5$	
0.11	0.572	-3.446	0.016	1.099	

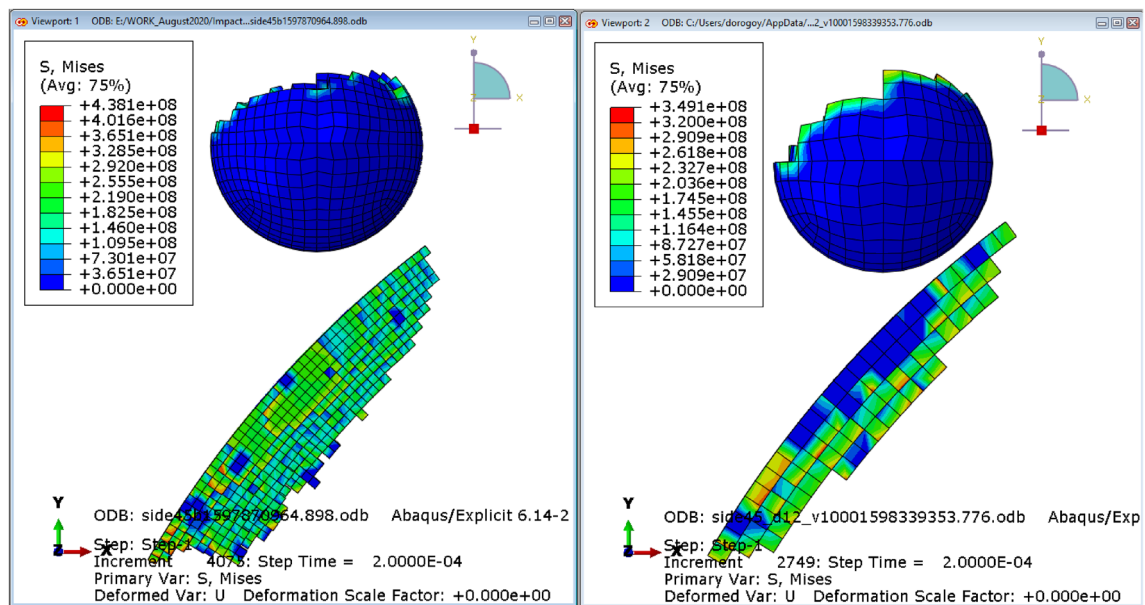


**Fig. 12** The failed elements due to usage of regular mesh (right) and finer mesh (left). The mass of the failed elements on the left of Fig. 12 is 3.32 gr. The mass of the failed elements on the right is: 3.51 gr, i.e., a difference of 5.4%

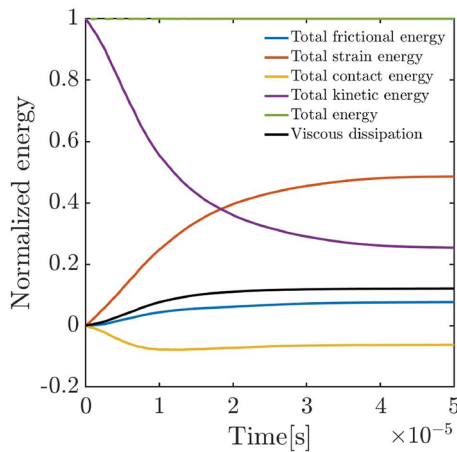


Fig. 13 Energy distribution

## Appendix A: Mesh Convergence Test for Non-Symmetric Impact (Oblique Impact)

The meshed geometry is shown on the upper part of Fig. 11. The regular mesh is on the right side and the finer mesh is on the left side. The bottom figures show a detail near the impact location which emphasize the mesh differences. An off-center impact at  $\theta = 45^\circ$  with impact velocity of 1000 m/s is modeled.

The mesh seed size of the “regular mesh” is 1 mm for the sphere and the hollow cylinder near the impact location. The mesh is comprised of 113,546 nodes and 96,396 elements of type C3D8R.

The mesh seed size of the “fine mesh” is 0.75 mm for the sphere and 0.5 mm for the hollow cylinder near the impact location. The mesh is comprised of 552,864 nodes and 506,616 elements of type C3D8R. The finer mesh contains 5.25 times more elements than the regular one.

The undeformed elements which were removed from the analysis due to failure are shown in Fig. 12. The failed elements due to analysis with regular mesh are shown on the right. The failed elements due to analysis with the finer mesh are shown on the left.

Although the volume of the target elements in the fine mesh is 8 times smaller than the regular mesh the difference in the damaged (failed) elements’ mass is only 2.9%. The difference in the remaining normalized kinetic energy of the sphere is ~4%. We see this accuracy as sufficient for this descriptive work, that has the purpose of raising a hitherto unstudied aspect of damage to shells and pipes.

## Appendix B: Material Model Parameters for Aluminum 7075 T651

The Johnson–Cook material model with the Mie–Gruneisen equation of state which we successfully used recently for hypervelocity impacts [12] was utilized.

The parameters set for the Johnson–Cook (JC) material model and the Johnson–Cook dynamic failure are based on the literature [13–15] and MATWEB (<http://www.matweb.com/search/>), see Table 4.

Using Young’s Modulus  $E = 71.7$  GPa and  $\rho = 2810$  kg/m<sup>3</sup> (from MATWEB) the parameters used for the Mie–Gruneisen EOS for Aluminum 7075-T651 are [16, 17]: Gruneisen coefficient,  $\Gamma_0 = 2.0$ , Wave speed,  $c_0 = 5051$  m/s and parameter  $s = 1.34$ .

## Appendix C

The simulation of normal impact of a sphere having a diameter of 12 mm at 1000 m/s on a hollow cylinder with thickness of 6 mm and outer diameter of  $D = 120$  mm will serve as an example for the energy partition.

Abaqus considers several types of energies, as listed below:

ETOTAL: Energy balance. (Available only for the whole model).

ALLKE: Kinetic energy.

ALLIE: Total strain energy.

ALLVD: Energy dissipated by viscous effects.

ALLFD: Total energy dissipated through frictional effects. (Available only for the whole model).

ALLIHE: Internal heat energy.

ALLWK: External work. (Available only for the whole model).

ALLPG: Energy added by particle generators. (Available only for the whole model.)

ALLPW: Work done by contact penalties, including general contact and penalty/kinematic contact pairs. (Available only for the whole model.)

ALLCW: Work done by constraint penalties. (Available only for the whole model.)

ALLMW: Work done in propelling mass added in mass scaling. (Available only for the whole model.)

ALLHF: External heat energy through external fluxes.

During the analysis the total energy remains constant. The energy balance (ETOTAL) is defined in ABAQUS as:

$$\begin{aligned}
 ETOTAL = & ALLKE + ALLIE + ALLVD + ALLFD \\
 & + ALLIHE + ALLWK - ALLPG - ALLPW \\
 & - ALLCW - ALLMW - ALLHF
 \end{aligned}$$

The energy balance simplifies to the following expression when only relevant terms are retained:

$$ETOTAL = ALLKE + ALLIE + ALLVD + ALLFD - ALLPW$$

These energies are plotted vs. time in Fig. 13. ETOTAL remains constant during the analysis and its value is the initial kinetic energy of the sphere.

**Acknowledgements** We thank the MADRI research center at Technion for support and Dr. A. Dorogoy for helping with the numerical simulations.

**Funding** The study was supported by PMRI-Technion (PMRI 907141).

## References

- Rosenberg Z, Dekel E (2020) Terminal ballistics. Springer, Berlin. <https://doi.org/10.1007/978-3-030-46612-1>
- Corbett GG, Reid SR, Johnson W (1996) Impact loading of plates and shells by free-flying projectiles: a review. *Int J Impact Eng* 18:141–230. [https://doi.org/10.1016/0734-743X\(95\)00023-4](https://doi.org/10.1016/0734-743X(95)00023-4)
- Ben-Dor G, Dubinsky A, Elperin T (2005) Ballistic impact: recent advances in analytical modeling of plate penetration dynamics—a review. *Appl Mech Rev*. <https://doi.org/10.1115/1.2048626>
- Børvik T, Langseth M, Hopperstad OS, Malo KA (1999) Ballistic penetration of steel plates. *Int J Impact Eng* 22:855–886. [https://doi.org/10.1016/S0734-743X\(99\)00011-1](https://doi.org/10.1016/S0734-743X(99)00011-1)
- Jonas GH, Zukas JA (1978) Mechanics of penetration: analysis and experiment. *Int J Eng Sci* 16:879–903. [https://doi.org/10.1016/0020-7225\(78\)90073-3](https://doi.org/10.1016/0020-7225(78)90073-3)
- Anderson CE, Bodner SR (1988) Ballistic impact: the status of analytical and numerical modeling. *Int J Impact Eng* 7:9–35. [https://doi.org/10.1016/0734-743X\(88\)90010-3](https://doi.org/10.1016/0734-743X(88)90010-3)
- Backman ME, Goldsmith W (1978) The mechanics of penetration of projectiles into targets. *Int J Eng Sci* 16:1–99. [https://doi.org/10.1016/0020-7225\(78\)90002-2](https://doi.org/10.1016/0020-7225(78)90002-2)
- ABAQUS (2020) Abaqus analysis user's guide. Simulia, Dassault Systemes
- Wen HM, Reid SR (1998) Deformation and perforation of cylindrical shells struck normally by blunt projectiles. *Int J Press Vessel Pip* 75:213–219. [https://doi.org/10.1016/S0308-0161\(98\)00024-6](https://doi.org/10.1016/S0308-0161(98)00024-6)
- Xiaoqing M, Stronge WJ (1985) Spherical missile impact and perforation of filled steel tubes. *Int J Impact Eng* 3:1–16. [https://doi.org/10.1016/0734-743X\(85\)90021-1](https://doi.org/10.1016/0734-743X(85)90021-1)
- Piekutowski AJ, Poormon KL (2008) Impact of thin aluminum sheets with aluminum spheres up to 9 km/s. *Int J Impact Eng* 35:1716–1722. <https://doi.org/10.1016/j.ijimpeng.2008.07.023>
- Dorogoy A, Rittel D, Weihs D (2020) Effect of target velocity on damage patterns in hypervelocity glancing collisions. *Int J Impact Eng* 144:103664. <https://doi.org/10.1016/j.IJIMPENG.2020.103664>
- Brar NS, Joshi VS, Harris BW (2009) Constitutive model constants for Al7075-T651 and Al7075-T6. *AIP Conf. Proc.*, vol. 1195, American Institute of Physics AIP; 2009, pp 945–948. doi:<https://doi.org/10.1063/1.3295300>.
- Børvik T, Hopperstad OS, Pedersen KO (2010) Quasi-brittle fracture during structural impact of AA7075-T651 aluminium plates. *Int J Impact Eng* 37:537–551. <https://doi.org/10.1016/j.ijimpeng.2009.11.001>
- Senthil K, Iqbal MA, Chandel PS, Gupta NK (2017) Study of the constitutive behavior of 7075–T651 aluminum alloy. *Int J Impact Eng* 108:171–190. <https://doi.org/10.1016/j.ijimpeng.2017.05.002>
- Lin Q, Li B (2020) Numerical simulation of dynamic large deformation and fracture damage for solid armature in electromagnetic railgun. *Def Technol* 16:348–353. <https://doi.org/10.1016/j.dt.2019.05.020>
- Jung J, Cho YJ, Kim SH, Lee YS, Kim HJ, Lim CY et al (2020) Microstructural and mechanical responses of various aluminum alloys to ballistic impacts by armor piercing projectile. *Mater Charact*. <https://doi.org/10.1016/j.matchar.2019.110033>

**Publisher's Note** Springer Nature remains neutral with regard to jurisdictional claims in published maps and institutional affiliations.